



Multilateral characterization for industrial Ziegler–Natta catalysts toward elucidation of structure–performance relationship



Toshiaki Taniike, Toshiki Funako, Minoru Terano*

School of Materials Science, Japan Advance Institute of Science and Technology, 1-1 Asahidai, Nomi, Ishikawa 923-1292, Japan

ARTICLE INFO

Article history:

Received 28 September 2013

Revised 29 October 2013

Accepted 30 October 2013

Keywords:

Ziegler–Natta catalyst

Magnesium diethoxide

Olefin polymerization

Multilateral characterization

Structure–performance relationship

ABSTRACT

High-performance Ziegler–Natta catalysts with ill-defined structural hierarchy were studied over multi-length scales. In this study, multilateral characterization was performed to address quantitative structure–performance relationships in ethylene/1-hexene copolymerization with $\text{Mg}(\text{OEt})_2$ -based Ziegler–Natta catalysts. Macroscopic characteristics of the catalysts (e.g., particle size and meso- and macropore volumes) were greatly affected by structures of $\text{Mg}(\text{OEt})_2$ precursor particles, while microscopic characteristics (e.g., micropore volume and chemical composition) were hardly influenced. Ethylene/1-hexene copolymerization results suggested the significance of monomer diffusion: The activity was enhanced for smaller catalyst particles, while the 1-hexene incorporation was improved with larger meso- and macropore volumes.

© 2013 Elsevier Inc. All rights reserved.

1. Introduction

“Multi-components” and “structural hierarchy” are the key issues to realize multifunctional and performant heterogeneous catalysts. The word, multi-components, represents that active components, support materials, modifiers, and cocatalysts in a system play different roles, while “structural hierarchy” dictates the significance of the structural design over multi-length scales. The most illuminative example, the three-way catalyst [1,2] for automotive catalytic converters typically consists of cordierite honeycomb support, whose structure is optimized to enhance the contact efficiency without penalizing airflow resistance, and a few-micron-thick washcoats deposited on the support. The washcoat consists of BaO-stabilized porous $\gamma\text{-Al}_2\text{O}_3$ as a carrier, CeO_2 ($/\text{ZrO}_2$) as an attenuator for the oscillation of the air-to-fuel ratio, and nano-sized noble metal or metal alloy (Pt/Pd/Rh) as active catalytic materials [1,3,4]. These multifunctional catalysts have been invented and developed mainly in an empirical manner from viewpoints of performance optimization in terms of activity, selectivity catalytic lifetime, and so on. In most of cases, roles of each component and impacts of each structural factor on the whole catalytic performance are roughly or qualitatively understood, while it is still challenging to embody quantitative structure–performance relationships (SPR) [5–7]. The difficulty comes from several reasons: A catalyst performance is usually affected by several chemical and structural factors in a complicated way, while to vary one

of these factors without changing the other factors is not easy in usual preparation procedures [8,9]. Furthermore, prepared catalysts contain different extents of chemical and structural heterogeneity over multi-length scales, making it extremely demanding to parameterize all factors that affect a catalytic performance [4,10].

The heterogeneous Ziegler–Natta catalyst for industrial olefin polymerization is a representative example of such catalysts. Manufacturing high-quality polymer products under efficient plant operation generally requires for a catalyst to simultaneously fulfill various performances such as high activity at an elevated temperature, (extremely) high selectivity, an appropriate kinetic profile, uniform particle sizes with spherical morphology, high hydrogen response for the polymer molecular weight control, and so on [11–13]. While there is a huge variety of preparation routes empirically established in terms of performance optimization [14], Ziegler–Natta catalysts at the level of industry generally possess the following structural features.

- (1) Pro-catalysts consist of TiCl_4 and a Lewis basic compound co-supported on activated MgCl_2 support, where the Lewis base called as internal donor is a key component to drastically improve the catalyst stereospecificity as well as to activate the MgCl_2 support during preparation [13,15–17].
- (2) Catalyst macroparticles possess spherical morphology with narrow particle size distributions typically between 10 μm and 100 μm . They are made by hierarchical agglomeration of primary structural units of TiCl_4 /internal donor/ MgCl_2 , whose dimensions are believed to be around 1–10 nm [18,19].

* Corresponding author. Fax: +81 761 51 1625.

E-mail address: terano@jaist.ac.jp (M. Terano).

- (3) The said hierarchical agglomeration leads to the formation of a range of porosity from micro to macropores, whose distributions and shapes are sensitively affected by employed preparation methods and conditions [20]. In Ziegler–Natta olefin polymerization, polymer initially formed in accessible pores build up mechanical stresses inside catalyst particles to trigger particle fragmentation (called the pore-breakage process), in which fresh catalyst surfaces which are originally hidden in inaccessible pores are continuously exposed. These processes enable industrial catalysts to retain stable polymerization activity over hours. In this way, inner structures of catalyst macroparticles significantly affect the fragmentation process [21,22] and the kinetic behavior during polymerization [12].

Roughly speaking, the first structural feature at the atomic scale is mainly related to the primary structure and polydispersity of produced polymer through the performance of active sites [14,23], while the latter two at larger scales from nm to μm mainly affect the kinetic profile of a catalyst and the resultant polymer particle morphology through fragmentation and replication phenomena during polymerization [11,24,25]. However, from a quantitative viewpoint, all these issues are believed to more or less exert influence on each said performance.

Though several research studies have been undertaken with the aim to understand relationships between catalyst structures and performances in Ziegler–Natta olefin polymerization, quantitative structure–performance relationships have not yet been reached. One of the main drawbacks in the previous studies can be attributed to the absence of multilateral characterization: They determined only one or a few structural parameter(s) of catalyst samples such as the crystalline disorder of MgCl_2 [26], surface area [27], total pore volume [12,28], and average pore size [12], without considering other parameters which also affect a targeted performance. Characterization and parameterization of the structures of Ziegler–Natta catalysts are actually not trivial in terms of the complexity and heterogeneity in chemical and physical structures as well as of their extreme sensitivity to moisture. Nevertheless, reliable quantitative structure–performance relationships are not to be acquired without parameterizing catalyst structures as precisely as possible with various characterization methods.

Based on these backgrounds, we have set as our primary objective to first establish and apply multilateral characterization for structures of Ziegler–Natta catalysts. Four catalysts were prepared based on the chemical conversion of $\text{Mg}(\text{OEt})_2$ precursor, which is one of the most commonly employed preparation routes in industry due to superior activity and copolymerization ability of resultant catalysts. They were subjected to a variety of characterization methods in order to achieve structural parameterization over multi-length scales such as electron microscopy, N_2 adsorption/desorption, Hg intrusion, UV/vis spectroscopy, and gas chromatography. We also examined impacts of the determined structural parameters on the ethylene/1-hexene copolymerization ability of the catalysts.

2. Experimental

2.1. Materials

Anhydrous MgCl_2 , triethylaluminum (TEA), and four kinds of poreless Mg particles (termed Mg A–D) were donated from Toho Titanium Co., Ltd., Tosoh Finechem Corporation and Yuki Gousei Kogyo Co., Ltd., respectively. The morphologies of Mg A,C are flake-like, while those of Mg B,D are spherical (Fig. 1). Character-

ization results of the Mg particles are shown in Table 1. The size of Mg particles becomes smaller in the order of $A \rightarrow C \rightarrow B \rightarrow D$.

Ethanol (purity >99.5%) was dried over 3A molecular sieve with N_2 bubbling. Heptane (purity >99.5%), toluene (purity >99.5%) and di-*n*-butylphthalate (DBP) (purity >98%) were dried over 4A molecular sieve with N_2 bubbling. Cyclohexylmethyldimethoxysilane (CMDMS) was purified by distillation under reduced pressure. Ethylene of research grade donated by Sumitomo Chemical Co., Ltd. was used as delivered.

2.2. $\text{Mg}(\text{OEt})_2$ synthesis

$\text{Mg}(\text{OEt})_2$ was synthesized based on a patent [29] with several modifications. 0.25 g of MgCl_2 (as an initiator) and 31.7 mL of dehydrated ethanol were introduced into a 500 mL jacket-type separable flask equipped with a mechanical stirrer rotating at 180 rpm under N_2 atmosphere. After the dissolution of MgCl_2 at 75 °C, 2.5 g of Mg and 31.7 mL of ethanol were introduced. 2.5 g of Mg and 31.7 mL of ethanol were again added 10 min after the reaction was initiated by MgCl_2 . Thereafter, 2.5 g of Mg and 31.7 mL of ethanol were added repeatedly 4 times every 10 min, followed by aging at 75 °C for 2 h. Finally, the temperature was decreased to 40 °C, and the product was washed with ethanol. In this study, four kinds of $\text{Mg}(\text{OEt})_2$ particles (MGE A–D) were synthesized from Mg A–D under the same conditions.

2.3. Catalyst preparation

The preparation of Ziegler–Natta catalysts from $\text{Mg}(\text{OEt})_2$ was conducted again based on a patent [30] with several modifications. 10 g of $\text{Mg}(\text{OEt})_2$ and 140 mL of toluene were charged in a 300 mL 3-neck flask equipped with a mechanical stirrer rotating at 180 rpm under N_2 atmosphere. 20 mL of TiCl_4 was added dropwise, while the temperature of the suspension was kept within 0–5 °C. Thereafter, the temperature was first elevated to 90 °C to add 3.0 mL of DBP, and then, it was brought to 110 °C. The reaction slurry was continuously stirred at 110 °C for 2 h. Subsequently, the reaction product was washed with toluene twice at 90 °C and further treated with 20 mL TiCl_4 at 90 °C for 2 h. After that, the product was washed with *n*-heptane 7 times to get the final catalyst. Four kinds of Ziegler–Natta catalysts (Cat A–D) were obtained from MGE A–D under the same conditions.

2.4. Polymerization

Ethylene/1-hexene copolymerization was performed in a 1 L autoclave equipped with a mechanical stirrer rotating at 350 rpm. 407 mL of *n*-heptane was introduced into the reactor. TEA ([Al] = 10 mmol/L), CMDMS (Al/E \times D = 10) and 93 mL of 1-hexene (corresponding to 0.75 mol) were introduced into the reactor, and the solution was saturated with 0.5 MPa of ethylene at 50 °C. A catalyst ([Ti] = 0.005 mmol/L) was fed into the reactor by a bomb injection technique to initiate the polymerization. The polymerization was conducted for 30 min with a continuous supply of ethylene gas at 0.5 MPa. The polymer was recovered by pouring the reaction slurry into mixture of acetone and methanol kept at 0 °C and subsequent filtration.

2.5. Characterization

2.5.1. Scanning electron microscopy

Particle morphological characteristics of $\text{Mg}(\text{OEt})_2$ and catalyst particles were studied with scanning electron microscopy (SEM, Hitachi S-4100) operated at an accelerating voltage of 20 kV. Before the measurements, particles were subjected to Pt sputtering for 100 s. To quantify observed particle morphology, SEM images

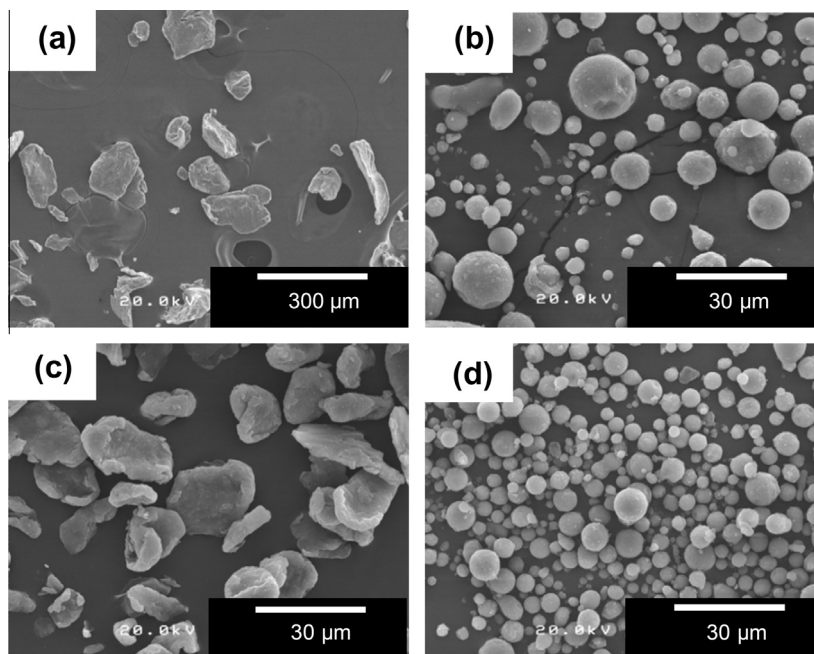


Fig. 1. SEM images of Mg particles: (a) Mg A ($\times 100$), (b) Mg B ($\times 1000$), (c) Mg C ($\times 1000$), and (d) Mg D ($\times 1000$).

Table 1
Characterization results of Mg particles.

Sample	D_{10}^a (μm)	D_{50}^a (μm)	D_{90}^a (μm)	RSF ^b
Mg A	15.7	39.7	132	2.93
Mg B	5.15	10.0	23.4	1.82
Mg C	7.94	17.2	28.6	1.78
Mg D	5.13	8.61	18.5	1.56

^a D_{10} , D_{50} and D_{90} are the particle diameters at 10%, 50% and 90% in the cumulative number-base particle size distribution obtained by the analysis of SEM images over 500 particles.

^b Determined based on Eq. (1).

(>500 particles) were analyzed by a software (Image J software, NIH). D_{10} , D_{50} , and D_{90} were defined as the particle diameters at 10%, 50%, and 90% in the cumulative number-based particle size distribution. The relative span factor (RSF) and the circularity degree were, respectively, calculated based on Eqs. (1) and (2),

$$\text{relative spanfactor (RSF)} = \frac{D_{90} - D_{10}}{D_{50}} \quad (1)$$

$$\text{circularity degree} = \frac{4 \times \pi \times \text{area}}{(\text{boundary length})^2} \quad (2)$$

where the area and boundary length for a two-dimensionally projected particle were determined over 500 particles.

2.5.2. N_2 adsorption/desorption measurement

N_2 adsorption and desorption isotherms at 77 K were acquired on a BELSORP-max instrument (BEL JAPAN, INC.). Ca. 50–100 mg of catalyst powder in a pyrex tube with a rubber cap was outgassed at 80 °C over 3 h in vacuo, prior to the measurement. Since the BET analysis is not appropriate for typical Ziegler–Natta catalysts with an abundance of micropores (pore diameter (D) < 2 nm) [17], the specific surface area was not determined. Instead, the micropore volume (V_{micro}) was approximated with the following

$$V_{\text{micro}} = V_{0.4} \times \frac{V_{\text{liquid}}}{V_{\text{gas}}} - \int_2^{50} \frac{2}{D} \cdot \frac{V_{\text{meso}}(D)}{dD} dD \quad (3)$$

where $V_{0.4}$, V_{liquid} , V_{gas} , and $V_{\text{meso}}(D)$ are the N_2 adsorption volume at $p/p_0 = 0.4$, the volumes of a N_2 molecule in gaseous and liquid states, and the mesopore volume at the diameter of D nm determined by the method described in the next paragraph. V_{micro} was estimated by subtracting the contribution of multilayer N_2 adsorption onto mesopore surfaces from the adsorption volume at $p/p_0 = 0.4$ (converted to the liquid N_2 volume). Note that the thickness of the multilayer adsorption at $p/p_0 = 0.4$ was approximated as 2 nm, and the contribution from the multilayer adsorption onto macropore and external surfaces was regarded as negligible. The latter is true for typical industrial Ziegler–Natta catalysts, whose pore dimensions are mainly micro- and/or meso-scale(s).

The mesopore size distributions ($2.1 \text{ nm} < D < 50 \text{ nm}$) were analyzed by the BJH method or by the INNES method. Even though the two methods are based on the same Kelvin equation for the N_2 condensation, cylinder-type and slit-type mesopores are assumed in the BJH and INNES methods, respectively. Hence, the BJH method is suitable for the hysteresis types H1 and H2, respectively, for uniform size and irregular size cylindrical-type mesopores, while the INNES method for the types H3 and H4, respectively, for uniform size and irregular size slit-type mesopores.

2.5.3. Mercury intrusion measurement

The meso- and macropore size distributions ($7 \text{ nm} < \text{diameter} < 1000 \text{ nm}$) were measured by the mercury intrusion technique (Pascal 440 Porosimeter, Thermo Scientific). The pore size was evaluated from the intrusion pressure according to the Washburn–Laplace equation. The surface tension (γ) and contact angle (θ) were, respectively, set to 0.480 N/m and 141.3.

2.5.4. Chemical analysis

The Ti content was determined by UV–vis spectroscopy (V-670 JASCO), in which a measured amount of a catalyst sample was dissolved in HCl/H₂SO₄/H₂O₂ solution, and the intensity of a ligand metal charge transfer band at 410 nm was measured. The DNBP content was determined by IR spectroscopy (FT/IR-4100, JASCO): A measured amount of a catalyst sample was first dissolved in HCl solution, DNBP was fully phase transferred to *n*-heptane, and

finally, the carbonyl absorption band was integrated to determine the DNBP content.

2.5.5. ^{13}C NMR

The 1-hexene incorporation amount, *i.e.* *n*-Bu branch content, in ethylene/1-hexene copolymer was measured by ^{13}C NMR (Bruker 400 MHz) operating at 100 MHz with proton decoupling at 120 °C using 1,2,4-trichlorobenzene as a diluent and 1,1,2,2-tetrachloroethane- d_2 as an internal lock and reference.

3. Results and discussion

3.1. $\text{Mg}(\text{OEt})_2$ synthesis

Four kinds of $\text{Mg}(\text{OEt})_2$ particles were synthesized from different Mg particles (whose characteristics were given in Fig. 1 and Table 1). Their representative SEM images are shown in Fig. 2. The particles of four $\text{Mg}(\text{OEt})_2$ samples more or less possessed spherical shapes. However, spheroidal particles, which were probably formed by agglomeration of the spherical particles and/or fine particles ($<1\ \mu\text{m}$), were occasionally observed. Magnified images (Fig. 2c) revealed that the particles were composed by aggregation of thin plate-like building blocks, whose dimension and shape were highly inhomogeneous. The lateral dimension of the building blocks varied in the range of 100–1000 nm, and the thickness was about 10 nm. Among the four samples, MGE A,C were relatively spherical compared with MGE B,D. On the other hand, there was no quantitative difference in their surface textures.

The particle characteristics of the $\text{Mg}(\text{OEt})_2$ samples such as the particle size distribution and the circularity obtained from SEM images are summarized in Table 2. The average particle size (D_{50}) became in the order of $\text{MGE D} > \text{C} > \text{B} > \text{A}$. MGE A,C synthesized from flake-like Mg had higher circularity and narrower particle size distribution than MGE B,D synthesized from spherical Mg. Moreover, smaller flake-like or spherical Mg particles, respectively, led to larger MGE particles (*i.e.* $\text{MGE C} > \text{A}$ and $\text{MGE D} > \text{B}$). Tanase and coworkers proposed a particle growth mechanism in the $\text{Mg}(\text{OEt})_2$ synthesis that $\text{Mg}(\text{OEt})_2$ seed particles formed on Mg surfaces fall off from the surfaces and aggregate with each other to shape the macroscopic particle morphology [31]. According to the mechanism, it was thought that the morphological differences in the original Mg particles exert influence on the said detachment and agglomeration behavior of the seed particles through the viscosity (shear force) of the reacting slurry, and consequently,

Table 2
Particle characteristics for $\text{Mg}(\text{OEt})_2$.

Sample	D_{10} (μm)	D_{50} (μm)	D_{90} (μm)	RSF	Circularity degree ^a
MGE A	19.6	22.3	26.2	0.298	0.911
MGE B	12.1	26.1	35.7	0.904	0.828
MGE C	21.0	26.6	30.5	0.359	0.901
MGE D	26.6	36.8	46.9	0.554	0.847
MGE C'	21.2	27.7	31.4	0.370	0.915

^a Determined based on Eq. (2).

differentiate the particle size distribution and circularity. To the best of our knowledge, these are the first academic results for the influence of the reaction conditions on the morphology of formed $\text{Mg}(\text{OEt})_2$ particles. It is notable that additional experiments on MGE C' (reproduction of MGE C) proved quantitative reproduction not only for the analysis but also for the synthesis.

3.2. Catalyst characterization

3.2.1. Morphology evaluation

From the four $\text{Mg}(\text{OEt})_2$ samples, four catalysts were prepared using the same conditions, whose SEM images are shown in Fig. 3. The shapes and sizes of the catalyst particles approximately replicated those of the $\text{Mg}(\text{OEt})_2$ particles for each. Though the replication more or less held at the level of the building blocks, their corners and edges became smeared after the catalyzation. Thus, macroscopic structural features of the particles were more accurately replicated, while structures at a smaller scale likely underwent some variation. These tendencies were similar among the four catalyst samples.

Table 3 shows the results of the particle analyses for SEM images of the catalyst particles. Again, Cat C' prepared from MGE C' had particle characteristics similar to Cat C from MGE C, proving the reproducibility of the catalyst synthesis. The results in Table 3 are discussed in a comparative way with those in Table 2 to clarify correlations of the particle morphology between the $\text{Mg}(\text{OEt})_2$ and catalyst samples. The orders of the particle characteristics among the four samples were slightly altered. For example, D_{50} had the order of $\text{Cat B} > \text{D} > \text{C} > \text{A}$ compared to $\text{MGE D} > \text{C} > \text{B} > \text{A}$, RSF had the order of $\text{Cat B} > \text{D} > \text{C} > \text{A}$ compared to $\text{MGE B} > \text{D} > \text{C} > \text{A}$, and so on. The RSF values became larger for all of the samples after the catalyzation. Cat B,D in particular formed non-negligible amounts of fine and agglomerated particles, resulting in more broadening in

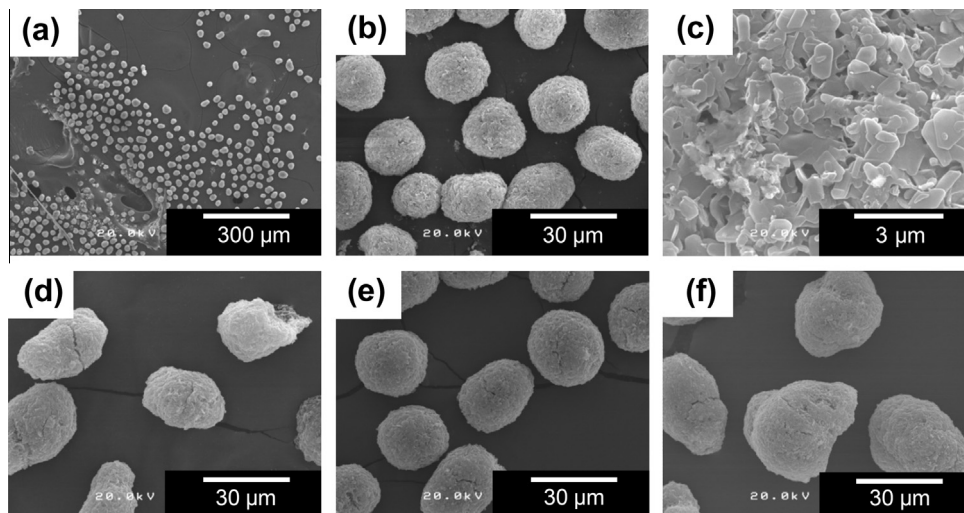


Fig. 2. SEM images of $\text{Mg}(\text{OEt})_2$ particles: (a) MGE A ($\times 100$), (b) MGE A ($\times 1000$), (c) MGE A ($\times 10000$), (d) MGE B ($\times 1000$), (e) MGE C ($\times 1000$), and (f) MGE D ($\times 1000$).

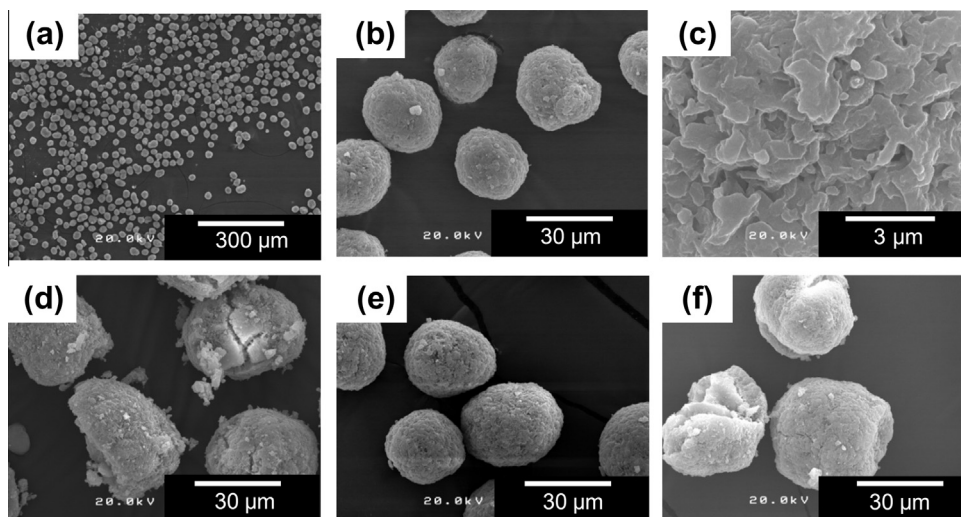


Fig. 3. SEM images of catalyst particles: (a) Cat A ($\times 100$), (b) Cat A ($\times 1000$), (c) Cat A ($\times 10000$), (d) Cat B ($\times 1000$), (e) Cat C ($\times 1000$), and (f) Cat D ($\times 1000$).

Table 3
Particle characteristics for catalysts.

Sample	SEM				
	D_{10} (μm)	D_{50} (μm)	D_{90} (μm)	RSF	Circularity degree
Cat A	22.3	25.6	31.0	0.343	0.835
Cat B	12.4	37.6	55.5	1.15	0.740
Cat C	26.8	30.9	41.9	0.490	0.896
Cat D	22.0	36.6	49.8	0.761	0.787
Cat C'	29.9	34.7	45.8	0.457	0.882

the particle size distribution compared with Cat A,C. It was believed that the particles of MEG A,C were mechanically tough probably because the plate-like morphology of Mg A,C might impose greater shear force during the particle formation. On the contrary, the particles of MEG B,D formed under lower shear force from the spherical Mg particles might be mechanically fragile, causing disintegration and re-agglomeration of the particles during the catalyst synthesis.

3.2.2. Pore structure evaluation

The catalyst pore structures were studied and compared based on N_2 adsorption and Hg porosimetry. N_2 adsorption is routinely employed not only for the determination of the (BET) specific surface area but also for the micro- and mesopore analyses [10]. On the other hand, Hg porosimetry is employed for the meso- and macropore analyses [32]. Cross-validation between the two pore analysis methods becomes possible by using overlapping dimensions of the two methods at the mesopore range.

Representative N_2 adsorption/desorption isotherms are shown for Cat C in Fig. 4 (the other samples had qualitatively similar isotherms). The adsorption isotherms for all the catalysts belonged to the type II of the IUPAC classification for macroporous ($D > 50$ nm) or non-porous materials. Meanwhile, the hysteresis loop made by the adsorption and desorption branches belonged to the type H3, suggesting the capillary condensation for slit-shaped mesopores ($2 \text{ nm} < D < 50 \text{ nm}$), whose sizes and shapes are non-uniform [33,34]. This is consistent with the lamellar morphology of the building blocks observed in SEM (Fig. 2c). The presence or absence of micropore filling ($D < 2$ nm) at low p/p_0 was not readily understandable from the isotherms, since it overlaps with the monolayer and multilayer adsorption. We have recently clarified by means of the α_s -plot method that typical Ziegler–Natta catalysts including $\text{Mg}(\text{OEt})_2$ -based catalysts contain at least two classes of micropores, which prevents reliable determination of the monolayer

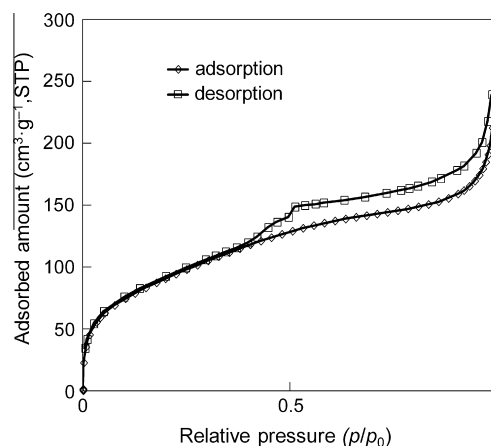


Fig. 4. Nitrogen adsorption/desorption isotherms for Cat C.

capacity in the BET surface area analysis [20]. Typical methods for the determination of the micropore volume or size distribution (such as HK and SF method) were not applicable to Ziegler–Natta catalysts either due to the absence of material-specific parameters for MgCl_2 or due to the continuity between the condensation micropore filling and mesopore filling in the adsorption isotherm [35,36]. Consequently, Eq. (3) was proposed as an intuitive method to estimate the micropore volume in Ziegler–Natta catalysts.

Fig. 5 represents the Hg intrusion data for Cat C (the other samples had similar intrusion curves). Typically for $\text{Mg}(\text{OEt})_2$ -based Ziegler–Natta catalysts, significant intrusion occurred at around 0.1 MPa. Comparison between the size scale for 0.1 MPa (10–20 μm) and a catalyst particle size (20–30 μm) dictates that the corresponding intrusion mainly arises from interparticle voids. After the intrusion into interparticle voids, second intrusion started at around 10 MPa, which was mainly due to intraparticle pores. Though it was not possible to clearly distinguish between the intrusion into interparticle voids and that into intraparticle pores, we have decided to regard the intrusion above 7.4 MPa (corresponding to below 200 nm) as one which mainly arose from intraparticle pores.

The INNES method [37] was employed for the mesopore analysis instead of the most popular BJH method [38]. The former assumes slit-type pores in agreement with the H3 hysteresis

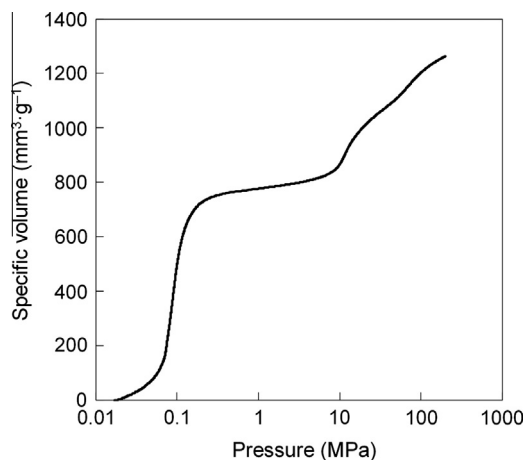


Fig. 5. Hg intrusion curve for Cat C.

observed for the catalysts (Fig. 4), while the latter assumes cylindrical pores. Fig. 6 compares the mesopore volumes obtained by the N_2 adsorption and Hg porosimetry in the range of $10 \text{ nm} < D < 50 \text{ nm}$ for the four catalysts. The INNES method for slit-type pores exhibited relatively good linear correlation with the pore volume determined by the Hg intrusion, while no correlation was detected for the BJH method. The deviation in the absolute volumes between the N_2 adsorption and the Hg intrusion came from different pore network filling mechanisms [39]. The Hg intrusion underestimates pore sizes in the presence of bottleneck pores within the pore network, while this is not the case for the N_2 adsorption. Thus, the meaning of $10 \text{ nm} < D < 50 \text{ nm}$ is not necessarily equivalent for the N_2 adsorption and Hg porosimetry.

The results of the analyses for the N_2 adsorption and Hg porosimetry are summarized in Table 4. As shown in Table 4, $Mg(OEt)_2$ -based Ziegler–Natta catalysts have a wide range of porosity from micro- to macropores. While the four catalysts exhibited quite similar pore volumes in the micropore region, the difference in the pore volume among Cat A–D became greater at a larger pore dimension. Compared with Cat B, D that were prepared from spherical Mg sources, Cat A, C that were prepared from flake-like Mg sources had larger pore volumes in the meso- and macropore regions. Since such a tendency was not observed at the stage of $Mg(OEt)_2$, it is reasonable to consider that the different meso- and macroporosity arose in the course of catalyzation. However,

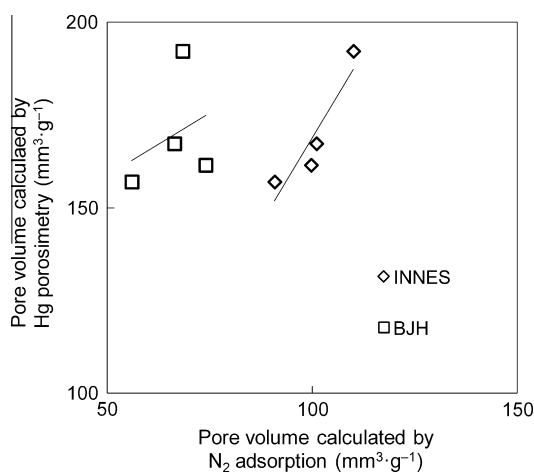


Fig. 6. Comparison of mesopore volumes ($10 \text{ nm} < D < 50 \text{ nm}$) between N_2 adsorption and Hg porosimetry. The mesopore volume for N_2 adsorption was analyzed either by the INNES or BJH method.

Table 4
Pore volumes for catalyst particles.

	Pore volume ($\text{mm}^3 \text{g}^{-1}$)		
	V_{micro} ($D < 2 \text{ nm}$) ^a	V_{meso} ($2 \text{ nm} < D < 50 \text{ nm}$) ^b	V_{macro} ($50 \text{ nm} < D < 200 \text{ nm}$) ^c
Cat A	111	194	216
Cat B	114	187	172
Cat C	112	196	220
Cat D	120	166	171

^a Calculated based on Eq. (3) from the N_2 adsorption isotherm.

^b Calculated by the INNES method from the N_2 adsorption isotherm.

^c Calculated based on the Washburn–Laplace equation from the Hg intrusion curve.

its mechanistic origin is unclear without capturing intermediate structures during the catalyzation.

3.3. Chemical composition

Table 5 summarizes the results of the chemical composition analyses. The chemical composition including the Ti and DNBP contents was not significantly different among Cat A–D, where the DNBP/Ti molar ratio always fell in a range of 1–1.2, typical for $Mg(OEt)_2$ -based Ziegler–Natta catalysts. Thus, macroscopic structural differences in $Mg(OEt)_2$ particles did not affect microscopic chemical parameters of the resultant catalysts, which enabled us to isolate influences of structural parameters on polymerization performance.

3.4. Ethylene/1-hexene copolymerization

In order to investigate correlations between catalyst structural parameters and polymerization performance, ethylene/1-hexene copolymerization was conducted. Though previous studies pointed out the significance of catalyst pore structures on the incorporation efficiency of bulky 1-hexene, quantitative examination has not yet been established [40]. The polymerization results are summarized in Table 6. The copolymerization activity was by far the highest for Cat A, and the remaining three showed the order of Cat C > B ~ D. Although it was considered that a variety of structural factors affected the activity, catalysts with smaller particle sizes tended to show higher activities (Fig. 7a). This fact plausibly suggests the importance of the diffusion limitation in ethylene polymerization:

Table 5
Chemical composition of catalysts.

	Ti contents (wt%)	DBP contents (wt%)
Cat A	2.4	17
Cat B	2.5	18
Cat C	2.7	18
Cat D	2.7	15

Table 6
Polymerization results^a.

Sample	Activity ($\text{kg-Ti} \cdot \text{mol}^{-1} \text{h}^{-1} \text{atm}^{-1}$)	<i>n</i> -Bu branch content ^b (mol%)
Cat A	1.5×10^3	6.3
Cat B	8.6×10^2	5.5
Cat C	1.1×10^3	6.3
Cat D	8.5×10^2	5.0

^a Ethylene/1-hexene copolymerization was conducted at 50 °C in heptane with 10 mmol/L of TEA, 1.0 mmol/L of CMDMS, 1.5 mol/L of 1-hexene, and 0.5 MPa of continuously supplied ethylene for 30 min.

^b Determined by ^{13}C NMR.

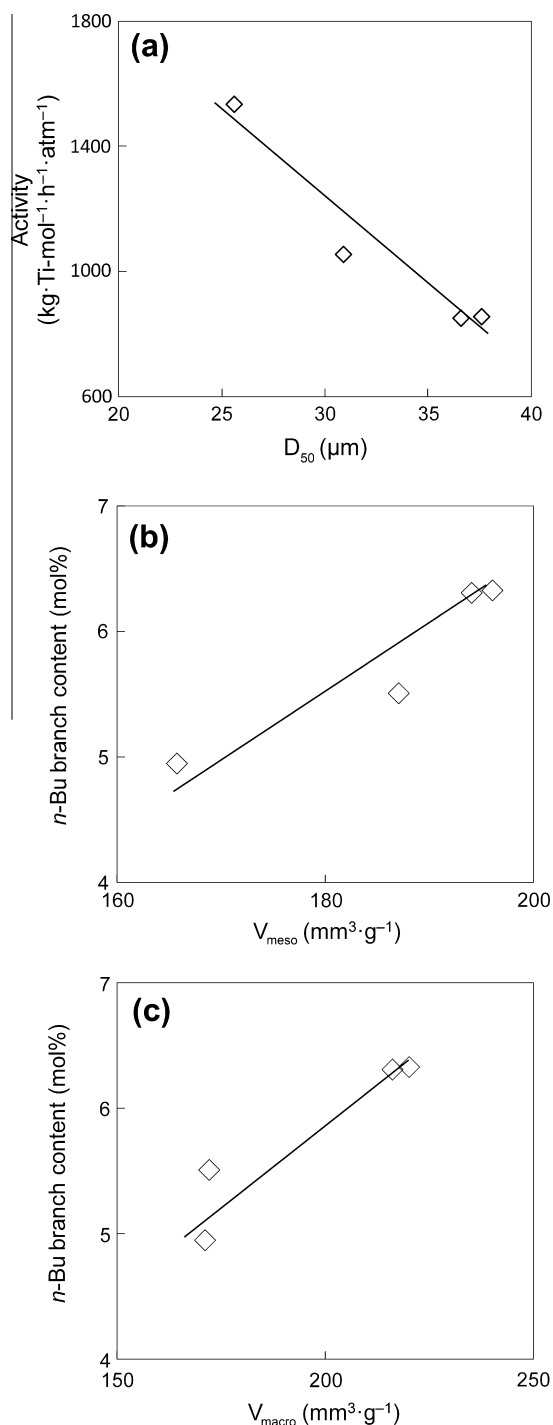


Fig. 7. Correlations between catalyst structural parameters and ethylene/1-hexene copolymerization performances: (a) D_{50} (number-base) vs. activity, (b) V_{meso} vs. *n*-Bu branch content, and (c) V_{macro} vs. *n*-Bu branch content.

When all the catalyst particles were covered by the polymer, smaller particles shorten the diffusion length of ethylene in the radial direction.

The 1-hexene incorporation efficiency followed the order of Cat C > A > B > D, in spite of the similarity of the catalyst composition, *i.e.* the active site nature. Since it was expected that the incorporation efficiency would be related to the ease of the diffusion for bulkier 1-hexene, the *n*-Bu branch contents were plotted against the pore-related parameters (Fig. 7b and c). Positive correlations were found for the mesopore volume determined by N_2 adsorption and for the macropore volumes by Hg intrusion. As reported in the

recent literature, accessible pores are readily filled by polymer formed at the very initial stage of polymerization (roughly corresponding to a few g-polymer/g-catalyst) [41]. Therefore, the pore volume is likely to exert its influence on the 1-hexene incorporation efficiency only at the initial stage. A possible scenario is as follows: At the initial timing of polymerization when catalyst pores are not yet filled, 1-hexene must reach active sites in competition with ethylene. Pores with the dimension comparable with the molecular size of 1-hexene decelerate its diffusion, and the number of pores with the dimension larger than the size of 1-hexene directly affects the 1-hexene incorporation at the initial stage. Copolymer formed at the initial stage fills accessible pores to become diffusion resistance at a later stage of polymerization. In general, the diffusion barrier becomes lower when the crystallinity of the polymer gets lower by the incorporation of more 1-hexene, subsequently leading to more 1-hexene incorporation even after the initial stage [42]. It was considered that the mesopore and macropore volumes affected the 1-hexene incorporation efficiency through the crystallinity of the initially formed polymer. The scenario is consistent with a known fact that the formation of less crystalline polymer in a pre-polymerization stage drastically enhances the α -olefin incorporation efficiency of a catalyst [43].

4. Conclusions

In this study, multilateral characterization was applied to state-of-the-art Ziegler–Natta catalysts featured with ill-defined hierarchical structures. Precise parameterization of the catalysts through scanning electron microscopy, Hg porosimetry, N_2 adsorption/desorption, and chemical analyses enabled us to tackle structure–performance relationships in heterogeneous olefin polymerization.

$\text{Mg}(\text{OEt})_2$ -based Ziegler–Natta catalysts possessed nearly spherical particle morphology, whose size distribution roughly replicated that of $\text{Mg}(\text{OEt})_2$ precursor particles. The catalyst particles contained a wide class of internal pores: macropores, slit-shaped mesopores, and micropores. Contrary to macroscopic parameters (particle size, macropore volume), microscopic parameters (micropore volume, chemical composition) were hardly affected by structures of $\text{Mg}(\text{OEt})_2$ particles. Among the chemical and structural parameters obtained, we found that the number-average particle size of the catalysts was negatively correlated with the activity in ethylene/1-hexene copolymerization, and that the meso- and macropore volumes were positively correlated with the 1-hexene incorporation efficiency. These two correlations suggested not only the importance of the monomer diffusion in ethylene/1-hexene copolymerization, but also the validity of multilateral characterization over multi-length scales to depict structure–performance relationships for such a complicated catalyst whose ill-defined hierarchical structure has been empirically optimized.

Acknowledgments

The Authors appreciate Sumitomo Chemical Co., Ltd., Toho Titanium Co., Ltd., Tosoh Finechem Corporation and Yuki Gousei Kogyo Co., Ltd. for the donation of reagents used in this study.

References

- [1] S. Matsumoto, *Catal. Today* 90 (2004) 183–190.
- [2] J. Kašpar, P. Fornasiero, M. Graziani, *Catal. Today* 50 (1999) 285–298.
- [3] H.S. Gandhi, G.W. Graham, R.W. McCabe, *J. Catal.* 216 (2003) 433–442.
- [4] R.M. Heck, R.J. Farrauto, *Appl. Catal. A: Gen.* 221 (2001) 443–457.
- [5] G. Occhipinti, H.R. Bjørsvik, V.R. Jensen, *J. Am. Chem. Soc.* 128 (2006) 6952–6964.
- [6] M.A. Peña, J.L.G. Fierro, *Chem. Rev.* 101 (2001) 1981–2017.
- [7] A. Corma, J.M. Serra, P. Serna, M. Moliner, *J. Catal.* 232 (2005) 335–341.
- [8] E.J. Dil, S. Pourmahdian, M. Vatakhah, F.A. Taromi, *Polym. Bull.* 64 (2010) 445–457.

- [9] J. Kim, M. Choi, R. Ryoo, *J. Catal.* 269 (2010) 219–228.
- [10] T. Tatsumi, N. Jappar, *J. Phys. Chem. B* 102 (1998) 7126–7131.
- [11] A. Dashti, S.A. Ramazani, Y. Hiraoka, S.Y. Kim, T. Taniike, M. Terano, *Polym. Int.* 58 (2009) 40–45.
- [12] M. Hassan Nejad, P. Ferrari, G. Pennini, G. Cecchin, *J. Appl. Polym. Sci.* 108 (2008) 3388–3402.
- [13] E. Albizzati, U. Giannini, G. Collina, L. Noristi, L. Resconi, in: E.P. Moore Jr. (Ed.), *Polypropylene Handbook*, Hanser-Gardner Publications, Cincinnati, OH, 1996 (Chapter 2).
- [14] Y. Hiraoka, S.Y. Kim, A. Dashti, T. Taniike, M. Terano, *Macromol. React. Eng.* 4 (2010) 510–515.
- [15] K.K. Kang, T. Shiono, Y.T. Jeong, D.H. Lee, *J. Appl. Polym. Sci.* 71 (1999) 293–301.
- [16] A. Andoni, J.C. Chadwick, H.J.W. Niemantsverdriet, P.C. Thüne, *J. Catal.* 257 (2008) 81–86.
- [17] T. Taniike, M. Terano, *J. Catal.* 293 (2012) 39–50.
- [18] R. Zannetti, C. Marega, A. Marigo, A. Martorana, *J. Polym. Sci. Part B: Polym. Phys.* 26 (1988) 2399–2412.
- [19] M. Kakugo, H. Sadatoshi, J. Sakai, in: T. Keii, T. Soga (Eds.), *Catalytic Olefin Polymerization*, H Kodansha-Elsevier, Tokyo, 1990, pp. 345–354.
- [20] T. Taniike, P. Chammingkwan, V.Q. Thang, T. Funako, M. Terano, *Appl. Catal. A: Gen.* 437–438 (2012) 24–27.
- [21] X. Zheng, M.S. Pimplapure, G. Weickert, J. Loos, *Macromol. Rapid Commun.* 27 (2006) 15–20.
- [22] X. Zheng, J. Loos, *Macromol. Symp.* 236 (2006) 249–258.
- [23] T. Wada, T. Taniike, I. Kouzai, S. Takahashi, M. Terano, *Macromol. Rapid Commun.* 30 (2009) 887–891.
- [24] T.F.L. McKenna, A.D. Martino, G. Weickert, J.B.P. Soares, *Macromol. React. Eng.* 4 (2010) 40–64.
- [25] P. Pokasermong, P. Praserttham, *Eng. J.* 13 (2009) 57–64.
- [26] P. Galli, P. Barbè, G. Guidetti, R. Zannetti, A. Martorana, A. Marigo, M. Bergozza, A. Fichera, *Eur. Polym. J.* 19 (1983) 19–24.
- [27] A. Marigo, C. Marega, R. Zannetti, G. Morini, G. Ferrara Euro, *Polym. J.* 36 (2000) 1921–1926.
- [28] L.A. Almeida, M.F.V. Marques, *Macromol. React. Eng.* 6 (2012) 57–64.
- [29] H. Nomura, N. Kurihara, K. Higuchi, JP Patent 1991-74341, 1991 (to COLCOAT Engineering Co., Ltd.).
- [30] M. Terano, A. Murai, M. Inoue, K. Miyoshi, JP Patent 1987-158704, 1987 (to Toho Catalyst Co., Ltd.).
- [31] S. Tanase, K. Katayama, S. Inasawa, F. Okada, Y. Yamaguchi, T. Konakazawa, T. Junke, N. Ishihara, *Appl. Catal. A: Gen.* 350 (2008) 197–206.
- [32] A. Martínez, G. Prieto, J. Rollán, *J. Catal.* 263 (2009) 292–305.
- [33] K.S.W. Sing, D.H. Everett, R.A.W. Haul, L. Moscou, R.A. Pierotti, J. Rouquérol, T. Siemienińska, *Pure Appl. Chem.* 57 (1985) 603–619.
- [34] K.S.W. Sing, *Pure Appl. Chem.* 54 (1982) 2201–2218.
- [35] J.H. de Boer, B.G. Linsen, T.J. Osinga, *J. Catal.* 4 (1965) 643–648.
- [36] N. Setoyama, T. Suzuki, K. Kaneko, *Carbon* 36 (1998) 1459–1467.
- [37] W.B. Innes, *Anal. Chem.* 29 (1957) 1069–1073.
- [38] E.P. Barrett, L.G. Joyner, P.P. Halenda, *J. Am. Chem. Soc.* 73 (1951) 373–380.
- [39] K.L. Murray, N.A. Seaton, M.A. Day, *Langmuir* 15 (1999) 8155–8160.
- [40] P. Kumkaew, L. Wu, P. Praserttham, S.E. Wanke, *Polymer* 44 (2003) 4791–4803.
- [41] T. Taniike, V.Q. Thang, N.T. Binh, Y. Hiraoka, T. Uozumi, M. Terano, *Macromol. Chem. Phys.* 212 (2011) 723–729.
- [42] C. Przybyla, B. Tesche, G. Fink, *Macromol. Rapid Commun.* 20 (1999) 328–332.
- [43] Y.S. Ko, S.I. Woo, *J. Polym. Sci. Part A: Polym. Chem.* 41 (2003) 2171–2179.